Materials Science & Engineering A 644 (2015) 318–324

Contents lists available at ScienceDirect

Materials Science & Engineering A

journal homepage: www.elsevier.com/locate/msea

Towards resolving the anonymity of pyramidal slip in magnesium

Haidong Fan [a,b,*], Jaafar A. El-Awady [a]

[a] Department of Mechanical Engineering, Johns Hopkins University, Baltimore, MD 21218, USA
[b] Department of Mechanics, Sichuan University, Chengdu, Sichuan 610065, China

ARTICLE INFO

Article history:
Received 7 May 2015
Received in revised form
20 June 2015
Accepted 26 July 2015
Available online 29 July 2015

Keywords:
Magnesium
Dislocations
Pyramidal slip
Molecular dynamics
Peierls stresses

ABSTRACT

Plasticity in magnesium crystals oriented for *c*-axis compression has been usually attributed to $\langle c+a\rangle$ dislocation slip on second-order pyramidal $\{11\bar{2}2\}$ planes. Through molecular dynamics simulations, we investigated the formation and slip characteristics of $\langle c+a\rangle$ dislocations on second-order pyramidal planes. It is shown that the critical *c*-axis compressive stress for these dislocations is almost seven times that for $\langle c+a\rangle$ dislocations on first-order pyramidal $\{10\bar{1}1\}$ planes. In particular, it is concluded that first-order pyramidal near-screw $\langle c+a\rangle$ dislocations play a predominant role during the *c*-axis compression of magnesium crystals. Careful reexaminations of published experimental observations show good agreements with the current predictions.

1. Introduction

Hexagonal closed packed (HCP) crystals are anisotropic in their mechanical properties, and mostly exhibit limited ductility [1]. Pyramidal slip has been shown to be very important for improving the ductility of polycrystalline HCP materials. Both titanium [2] and zirconium [3] demonstrate good ductility through commonly observed first-order pyramidal slip. Furthermore, the addition of yttrium in magnesium (Mg) was shown to remarkably improve ductility compared to pure Mg through a high activity of both first-order and second-order pyramidal slips [4].

While Mg and its alloys have been extensively studied over the past few decades, there is still an ongoing debate on the nature of pyramidal slip in these crystals. Many conflicting experimental results have contributed to the confusions on whether $\langle c+a\rangle$ dislocation slip is predominant on first-order pyramidal $\{10\bar{1}1\}$ (Pyramidal-I) or second-order pyramidal $\{11\,\bar{2}2\}$ (Pyramidal-II) planes. These confusions either originated from incorrect analysis, or claims without sufficient supporting evidences.

One of the most widely cited experiments suggesting Pyramidal-II $\langle c+a\rangle$ slip during *c*-axis loading of Mg is based on surface slip trace analysis by Obara et al. [5]. Fig. 1(a) shows a reproduction of those slip traces nearly on the $\{1\bar{1}00\}$ surface after 2.9% strain at room temperature [5]. The authors have identified the horizontal slip traces coincide with basal slip, and the inclined slip traces make an angle of 55° on average with respect to the basal plane. Based on this, the authors have suggested that these inclined lines coincide with Pyramidal-II slip traces within 5° error. Similar slip trace angles were reported for ZK60 [6] and pure Mg [7] and were also suggested to coincide with Pyramidal-II slip. As shown in Figs. 1(b), (c), and Appendix A, by simple geometric analysis of the HCP lattice, the ideal angles for slip traces of Pyramidal-I and Pyramidal-II planes on the $\{1\bar{1}00\}$ surfaces are in fact 58.4° and 39.1°, respectively. This indicates the reported slip traces in [5–7] probably coincide with Pyramidal-I slip, and not Pyramidal-II slip as commonly cited.

It should be noted that Pyramidal-II slip traces were recently reported during *c*-axis compression of bulk Mg crystals [8]. However, their slip trace observations were performed on samples before yielding, which could suggest they are a result of sample preparation.

Pyramidal-II slip was also passingly suggested to occur in both bulk [9] and micro [10] Mg crystals during *c*-axis compression, while based on TEM observations of *c*-axis compressed micropillars, it was suggested that $\langle c+a\rangle$ dislocations may be on Pyramidal-I planes [11]. However, these conclusions are mostly speculative without any conclusive evidences. In addition, in the drop hammer tests of single crystal Mg, only twinning deformation was reported to be effective for *c*-axis compression [12].

Molecular dynamics (MD) simulations have showed that during *c*-axis compression and tension, $\langle c+a\rangle$ dislocations predominantly nucleate on Pyramidal-I planes from free surfaces and cavities [13–15], while discrete dislocation dynamics (DDD)

* Corresponding author at: Department of Mechanical Engineering, Johns Hopkins University, Baltimore, MD 21218, USA.
E-mail addresses: haidongfan8@foxmail.com (H. Fan), jelawady@jhu.edu (J.A. El-Awady).

http://dx.doi.org/10.1016/j.msea.2015.07.080
0921-5093/

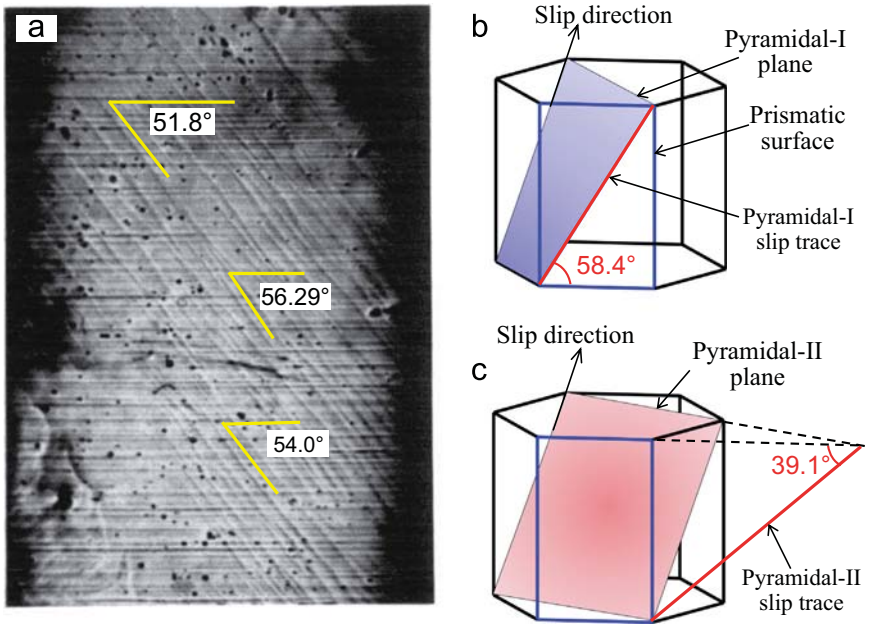

Fig. 1. (a) Slip bands nearly on $\{1\bar{1}00\}$ surface of a Mg single crystal after 2.9% compressive strain along the *c*-axis and at room temperature from Obara et al. [5]. Reprinted with permission from Elsevier Limited. (b, c) Schematics of slip trace angles of Pyramidal-I and Pyramidal-II planes on the $\{1\bar{1}00\}$ surface, respectively. See Appendix A for full schematics of all possible slip trace angles.

simulations support Pyramidal-II slip [16–18]. On the other hand, the transition of slip from Pyramidal-I to Pyramidal-II planes was shown to be plausible through cross-slip or cooperative slip at high applied stresses [13]. These results also agree with the analytical stochastic model proposed by Zhang et al. [19].

These disagreements in experiments and simulations indicate the necessity to critically reevaluate our understanding of pyramidal slip in Mg. This is particularly important since confusions over which slip plane is predominant can lead to inaccuracies in predicting the mechanical response of Mg and its alloys. As such, the aim of this study is to address the perplexing nature of pyramidal slip in magnesium.

2. Simulation methods

MD simulations are utilized to study dislocation slips on both Pyramidal-I and Pyramidal-II planes. These simulations are performed using the MD simulator LAMMPS [20]. Two modified embedded atom method (MEAM) potentials developed by Kim

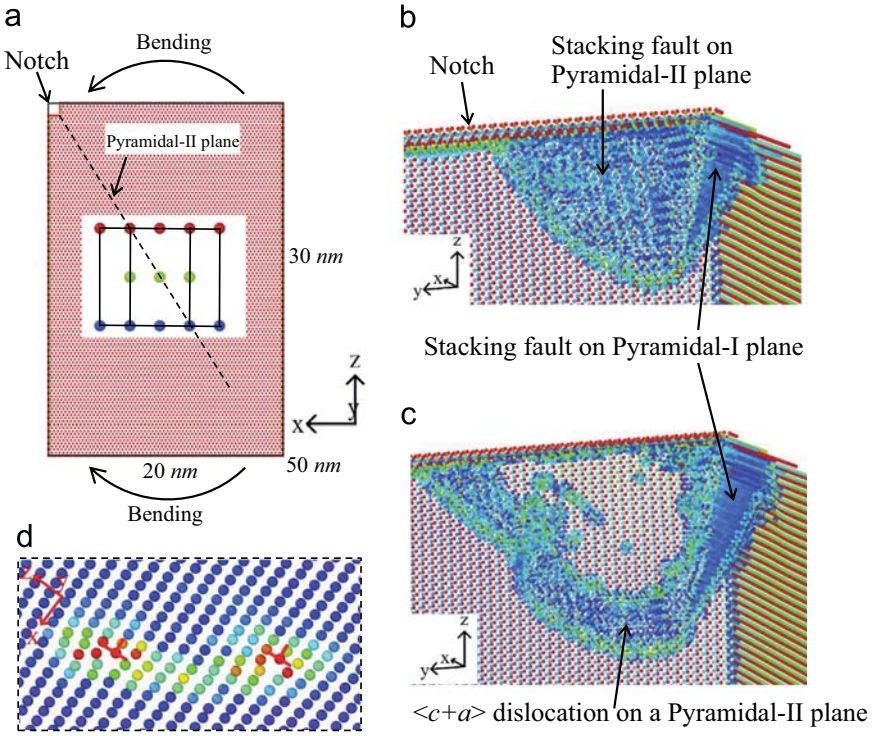

Fig. 2. Nucleation of Pyramidal-II $\langle c+a \rangle$ dislocations from free surfaces during bending simulations: (a) schematic of the simulation cell; (b, c) nucleating Pyramidal-II dislocations; and (d) the core of the nucleating Pyramidal-II $\langle c+a \rangle$ dislocation. The inverted "T" indicates the location of the leading and trailing partial dislocations.

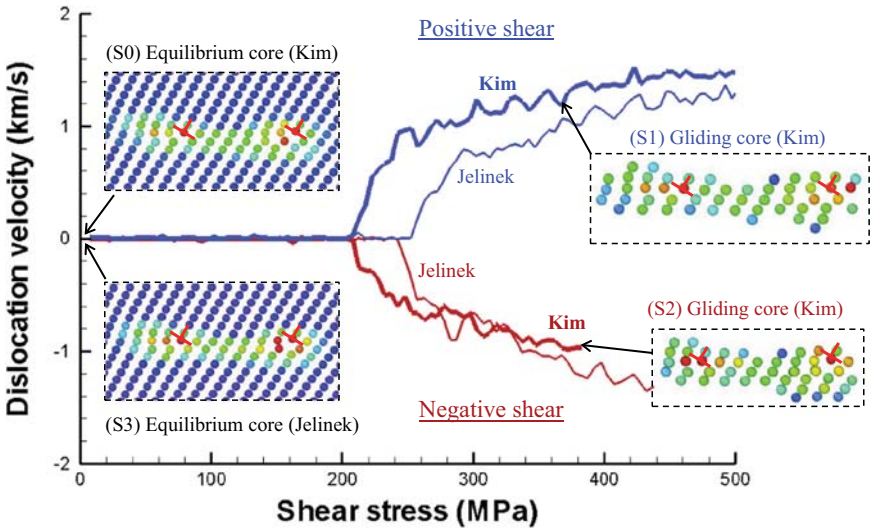

Fig. 3. Mobility curves for $\langle c+a\rangle$ edge dislocations on the Pyramidal-II plane. The thick lines are predicted using the Kim et al. potential [21], while the thin lines are predicted using the Jelinek et al. potential [22]. The red and blue curves indicate the response to negative and positive shear, respectively. The dislocation cores at zero load and during slip are shown in the insets, with the inverted "T" indicating the location of the leading and trailing partial dislocations. (For interpretation of the references to color in this figure legend, the reader is referred to the web version of this article.)

et al. [21] and Jelinek et al. [22] are used to model the interatomic interaction. The Kim potential was shown to be in good agreement with density functional theory (DFT) simulations, especially for the $\langle c+a\rangle$ dislocation cores [23]. All the atoms in this paper are visualized using OVITO [24].

Since Pyramidal-I slip was previously studied by the embedded atom method (EAM) potentials [13,25], Pyramidal-II slip is the main focus of the current work. Firstly, the surface nucleation of Pyramidal-II $\langle c+a\rangle$ dislocations is studied during bending of a rectangular simulation cell with edge lengths of 20 nm × 30 nm × 50 nm, as shown schematically in Fig. 2(a). Free surface boundary conditions are applied on all 3 directions. The crystal orientation is also shown in Fig. 2(a). A bending deformation is imposed by applying opposite rotation angles on the top and bottom ends, respectively. In addition, a notch is also introduced at the sample corner to accelerate dislocation nucleation. In the bending simulations, a normal stress is induced on the cross-section with its maximum on the outmost surfaces. Thus, the stress is highest at the notch, due to the induced stress concentration. As shown in Fig. 2(a), the notch edge resides fully on the Pyramidal-II plane. Therefore, Pyramidal-II slip would be more plausible.

In order to compare dislocation behaviors on Pyramidal-I versus Pyramidal-II planes, a second simulation cell with edge lengths 30 nm × 10 nm × 30 nm is adopted for simulations of both screw and edge Pyramidal-I and Pyramidal-II $\langle c+a\rangle$ dislocations. Periodic boundary conditions are imposed along both the dislocation line (parallel to the shortest edge) and glide directions, while free surface conditions are imposed along the directions normal to the slip plane. All the considered dislocations are introduced into this simulation cell by computing the anisotropic displacement field on all atoms in the simulation cell, followed by energy minimization. This leads to a dissociated dislocation under stress-free condition. A pure shear stress is imposed on the free surfaces of the simulation cell using a ramp loading with a stress rate of 1.0 MPa/ps. This was shown to greatly minimize the inertial effects that would develop within the sample [26]. The shear stress was applied using the NVE ensemble from a fully relaxed system. As such, the simulation cell temperature is less than 0.01 K before dislocation glide, and increases to less than 90 K due to plastic dissipation after dislocation glide. To identify any possible tension–compression asymmetry, the shear stress is imposed along two opposite directions for each dislocation. The positive shear denotes the deformation causing c-axis tension, while the negative shear denotes c-axis compression.

3. Results and discussions

In order to examine the possibility of $\langle c+a\rangle$ dislocations on Pyramidal-II planes, bending simulations are particularly performed, as shown in Fig. 2(a). Fig. 2(b) shows the instance just after the nucleation of two leading partial dislocations from the simulation cell corner, dragging two stacking faults behind them. Further examination of the two partial dislocations and connected stacking faults indicates that one nucleates exactly from the notch, and its slip plane coincides with a Pyramidal-II plane, as shown by the dashed line in Fig. 2(a). The other partial dislocation and stacking fault are observed to reside entirely on the Pyramidal-I plane, as indicated in Fig. 2(b). Due to the stress gradient from the bending deformation, the partial dislocation on the Pyramidal-I plane cannot glide further, whereas a trailing partial nucleates from the notch on the Pyramidal-II plane, leading to the formation of a full Pyramidal-II dislocation, as shown in Fig. 2(c). The nucleated dislocation core is shown in Fig. 2(d), and is planar on the Pyramidal-II plane. This dislocation core structure is identical to the $\langle c+a\rangle$ dislocation reported from DFT simulations of $\langle c+a\rangle$ dislocations on Pyramidal-II planes [23]. These bending simulations suggest that Pyramidal-II slip is plausible in Mg single crystals.

This $\langle c+a\rangle$ dislocation is subsequently introduced as an infinitely long dislocation into the second simulation cell, as discussed in Section 2, to identify the characteristics of Pyramidal-II $\langle c+a\rangle$ slip in terms of the Peierls stress and mobility. The dislocation velocity curves for an edge $\langle c+a\rangle$ dislocation on a Pyramidal-II plane is shown in Fig. 3. The stress-free equilibrium dislocation core as predicted by the Kim potential is shown in Fig. 3(S0). The dislocation core is planar on the Pyramidal-II plane, and the two edge partials are separated by $3.5b_{c+a}$, with b_{c+a} being the magnitude of the $\langle c+a\rangle$ Burgers vector. By identifying the atom positions, it is observed that this dislocation core is identical to those nucleating in the simulations under bending loads shown in Fig. 2 and those in DFT simulations [23]. Furthermore, the computed Peierls stress is 208 MPa for both positive and negative shear stresses, above which the edge dislocation glides in

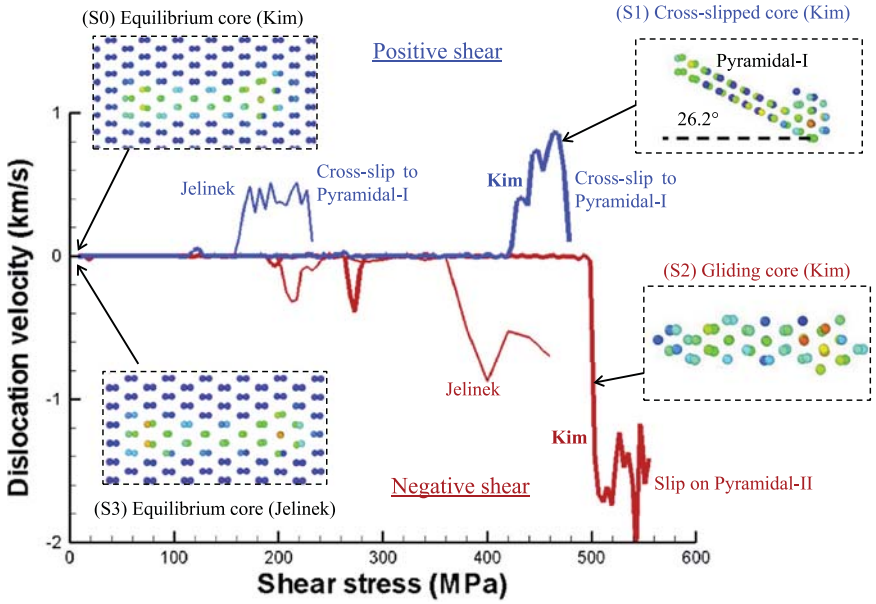

Fig. 4. Mobility curves for $\langle c+a\rangle$ screw dislocations on the Pyramidal-II plane. The thick lines are predicted using the Kim et al. potential [21], while the thin lines are predicted using the Jelinek et al. potential [22]. The red and blue curves indicate the response to negative and positive shear, respectively. The dislocation cores at zero load and during slip are shown in the insets. (For interpretation of the references to color in this figure legend, the reader is referred to the web version of this article.)

a smooth manner. With increasing applied shear stress, the dislocation velocity increases nonlinearly. The gliding cores under both positive and negative shear stresses are shown in Fig. 3(S1) and (S2). The cores are always stable and the velocity curves are very similar, indicating a weak tension–compression asymmetry.

To avoid the dependence of the results on a particular potential, the simulations were also performed using the Jelinek potential and the results are also shown in Fig. 3. The stress-free equilibrium dislocation core is shown in Fig. 3(S3), and is similar to that predicted by the Kim potential and DFT simulations [23]. The velocity curves are also similar to those predicted by the Kim potential, whereas the Peierls stress is 18% higher and equal to 247 MPa.

The dislocation velocity curves for the screw $\langle c+a\rangle$ dislocation on Pyramidal-II planes, as predicted by the Kim potential, are shown in Fig. 4. The stress-free equilibrium core is shown in Fig. 4 (S0), which disassociates into two $0.5\langle c+a\rangle$ partials. This core is similar to that predicted by DFT simulations [8]. The core is also planar on the Pyramidal-II plane. Under a positive applied shear stress, the screw dislocation is immobile on the Pyramidal-II plane up to a shear stress of 418 MPa. Subsequently, the screw dislocation cross-slips onto Pyramidal-I planes and glides smoothly until it exits the simulation cell from the free surface. The Pyramidal-I core after cross-slip is shown in Fig. 4(S1), and is identical to the un-shuffled core predicted in MD simulations using the EAM potentials [25]. The Peierls stress of pure screw dislocations on Pyramidal-I plane is much lower (i.e. 93 MPa [25]), which is probably the reason for the preferential cross-slip from Pyramidal-II to Pyramidal-I planes. Under a negative applied shear stress, the screw dislocation glides on the Pyramidal-II plane above a shear stress of 493 MPa. The gliding core is shown in Fig. 4(S2), and is always stable. However, its motion is rough, leaving behind large quantities of vacancies and interstitials. This rough motion is similar to that of screw dislocations in BCC iron crystals [27]. Comparing the screw dislocation responses under positive and negative shear stresses indicates a strong tension–compression asymmetry.

The simulation results for the screw dislocation on the Pyramidal-II plane as computed using the Jelinek potential are also shown in Fig. 4. The dislocation behaviors are similar to those predicted by the Kim potential. However, the Peierls stresses predicted here are slightly different. Under positive shear stress, the screw dislocation cross-slips to a Pyramidal-I plane at 157 MPa. Under negative shear stress, the dislocation begins gliding at 360 MPa, in a rough manner.

Pyramidal-I dislocation cores have been previously studied in details [25] using both the Sun et al. [28] and Liu et al. [29] EAM potentials. To facilitate comparisons with the current MEAM potential results, the Pyramidal-I dislocations are also studied here using the Kim potential. To guarantee periodic boundary conditions along both the dislocation slip and line directions, only the near-edge (i.e. along the $[2\,\bar{1}\,\bar{1}0]$ direction) and near-screw (i.e. along the $[01\bar{1}2]$ direction) dislocations are investigated, since the pure edge and screw dislocations cannot meet these conditions. All the Peierls stresses computed in this study for the Pyramidal-I and Pyramidal-II dislocations are summarized in Table 1. The Peierls stress for near-screw dislocations on Pyramidal-I planes is

Table 1
Peierls stress for Pyramidal-I and Pyramidal-II dislocations under pure shear stress (in MPa). The '+' and '−' signs denote positive and negative shear stresses. The dislocations shown in Fig. 5 are indicated here in bold.

	Pyramidal-I					Pyramidal-II			
	Kim et al. [21]		Liu et al. [29]			Kim et al. [21]		Jelinek et al. [22]	
	+	−	+	−		+	−	+	−
Near-edge	Sessile < 527	**Decompose422**	Glide 423	Glide 480	Edge	Glide 208	**Glide 208**	Glide 247	Glide 247
Near-screw	Glide 17	**Glide 27**	Glide 15	Glide 35	Screw	Cross-slip 418	**Glide 493**	Cross-slip 157	Glide 360

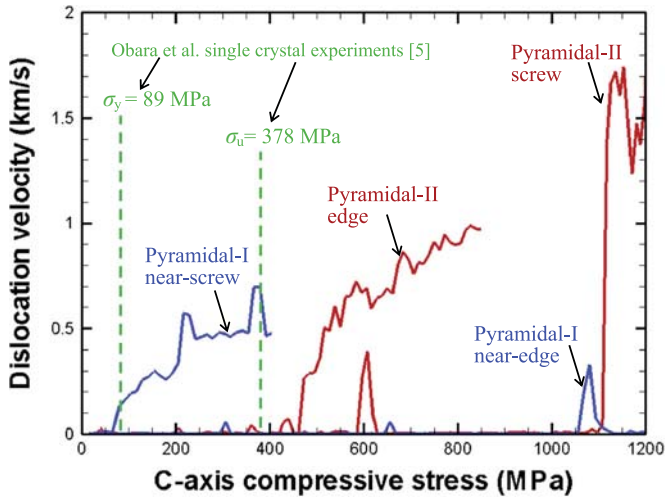

Fig. 5. Dislocation velocity for Pyramidal-I (blue) and Pyramidal-II (red) dislocations as a function of the *c*-axis compressive stress. All curves are computed using Kim et al. potential [21]. (For interpretation of the references to color in this figure legend, the reader is referred to the web version of this article.)

17 MPa for positive shear stress and 27 MPa for negative shear stress. These values agree well with predictions from the Liu potential (see Table 1). On the other hand, the near-edge dislocation stays sessile below a positive shear stress of 527 MPa. Under negative shear stress the dislocation is observed to decompose into $\langle c\rangle$ and $\langle a\rangle$ dislocations at 422 MPa.

Fig. 5 shows a direct comparison between the Pyramidal-I and Pyramidal-II dislocation velocities as a function of *c*-axis compressive stress. All the curves are computed using the Kim potential. The Peierls stresses of all the dislocations reported in Fig. 5 are indicated in bold in Table 1. The *c*-axis compressive stress is computed using Schmid factors equal to 0.4 and 0.45 on the Pyramidal-I and II planes, respectively. With increasing *c*-axis compressive stress, firstly, near-screw dislocations on Pyramidal-I planes begin gliding at a critical *c*-axis compressive stress of 68 MPa. Secondly, when the stress reaches 462 MPa the edge dislocations on Pyramidal-II planes will be activated. This critical *c*-axis compressive stress is almost ~7 times that for Pyramidal-I near-screw dislocations. Finally, the remaining two dislocation types are very difficult to be activated (i.e. critical stress > 1 GPa).

In addition, the yield and ultimate stresses as measured experimentally by Obara et al. [5] are 89 MPa and 378 MPa, respectively, and are also indicated in Fig. 5. By comparing these values to the dislocation slip activity, it is clear that during the plastic stage, only Pyramidal-I dislocations would be expected. This shows excellent agreement with the Pyramidal-I slip traces of Obara et al. [5] in Fig. 1. In particular, the experimental yield stress corresponds with the critical *c*-axis compressive stress for Pyramidal-I near-screw dislocations, which have a much smaller Peierls stress than all other pyramidal dislocations. Furthermore, edge dislocations were observed experimentally to be less mobile than screw dislocations [5], which again agrees with the current Pyramidal-I dislocations in Table 1. Based on the current MD simulations and direct comparisons with the experiments, it can be concluded that Pyramidal-I slip plays the major role during *c*-axis compression of Mg crystals.

To provide further rationale for the lower Peierls stress on Pyramidal-I plane, it is worth noting that the definition of the Peierls–Nabarro stress can be expressed as [30]

$$\tau_0 \propto \exp(-k\frac{d}{b}) \tag{1}$$

where *k* is a material constant, *d* is the interplanar spacing, and *b* is the magnitude of the Burgers vector. Thus, for $\langle c+a\rangle$ pyramidal slip, the Peierls stress is largely dependent on the interplanar spacing. The interplanar spacings of Pyramidal-I and Pyramidal-II planes are shown in Fig. 6. Through simple geometric calculations, the interplanar spacing of Pyramidal-II planes is equal to:

$$d_{\mathrm{II}} = \frac{ac}{2\sqrt{a^2+c^2}} = 0.426a. \tag{2}$$

On the other hand, as shown in Fig. 6(c), it is clear that the interplanar spacing of Pyramidal-I planes is not uniform, with the large spacing, $d_{\mathrm{I}}^{\mathrm{L}}$, being 5 times larger than the small spacing, $d_{\mathrm{I}}^{\mathrm{S}}$. As Tang and El-Awady [13] showed, slip would favorably occur between the large spaced planes, and the large spacing is equal to

$$d_{\mathrm{I}}^{\mathrm{L}} = \frac{5\sqrt{3}ac}{6\sqrt{3a^2+4c^2}} = 0.637a \tag{3}$$

This is obviously larger than the Pyramidal-II spacing, and thus a lower Peierls stress is expected here, which is in good agreement with the current MD predictions.

It should be noted that for micro- and nano-crystals, where the applied stress can be significantly higher than that in bulk crystals [31], slip might be activated on Pyramidal-II plane or both pyramidal planes, as previously shown during *c*-axis compression of nano-crystals [13].

4. Summary and conclusions

In summary, molecular dynamics simulations of $\langle c+a\rangle$ Pyramidal-I and Pyramidal-II dislocations show that the critical *c*-axis compressive stress for activation of Pyramidal-II slip is almost seven times that for Pyramidal-I slip. This indicates that Pyramidal-I slip, and in particular near-screw dislocations, play a major role during *c*-axis compression of Mg. Careful re-examinations of published experiments also support these conclusions. This work provides new insight in regards to pyramidal slip in

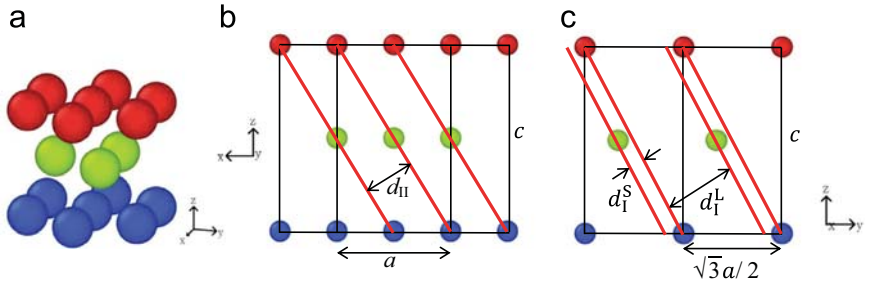

Fig. 6. The HCP lattice in magnesium. (a) 3D view of a unit cell; (b) $(1\bar{1}00)$ view of the Pyramidal-II planes; (c) $(11\bar{2}0)$ view of the Pyramidal-I planes.

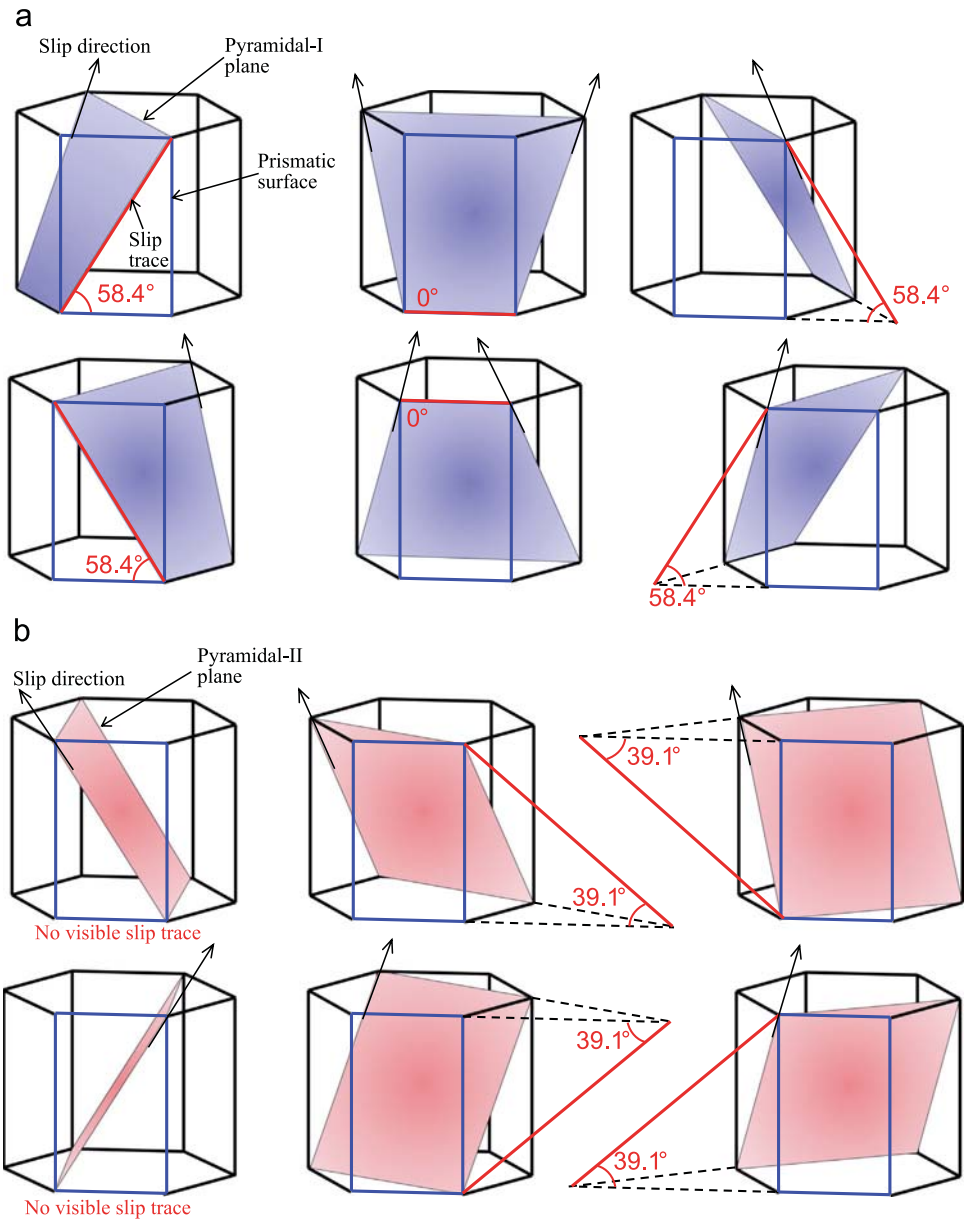

Fig. A1. Full schematics of the slip trace angles of (a) Pyramidal-I and (b) Pyramidal-II slips on the prismatic surface.

magnesium, which is of great importance for discrete dislocation dynamics [17–32] and crystal plasticity [33] simulations.

Acknowledgments

This research was sponsored by the Army Research Laboratory (#W911NF-12-2-0022). Views/conclusions contained here are those of the authors and should not be interpreted as representing the official policies, either expressed or implied, of ARL or U.S. Government. U.S. Government is authorized to reproduce and distribute reprints for Government purposes notwithstanding any copyright notation herein. HF also acknowledges the financial support of the National Natural Science Foundation of China (11302140), and Fundamental Research Funds for the Central Universities.

Appendix A

See Appendix Fig. A1.

References

[1] M.H. Yoo, Metall. Trans. A 12 (1981) 409–418.
[2] H. Numakura, Y. Minonishi, M. Koiwa, Scr. Metall. 20 (1986) 1581–1586.
[3] H. Numakura, Y. Minonishi, M. Koiwa, Philos. Mag. A 63 (1991) 1077–1084.
[4] S. Sandlöbes, M. Friák, J. Neugebauer, D. Raabe, Mater. Sci. Eng. A 576 (2013) 61–68.
[5] T. Obara, H. Yoshinga, S. Morozumi, Acta Metall. 21 (1973) 845–853.
[6] A. Galiyev, R. Kaibyshev, G. Gottstein, Acta Mater. 49 (2001) 1199–1207.
[7] J.-F. Stohr, P. Régnier, J.-M. Dupouy, Mém. Sci. Rev. Métall. LXVIII (1971) 49–54.
[8] T. Kitahara, S. Ando, M. Tsushida, H. Kitahara, H. Tonda, Key Eng. Mater. 345 (2007) 129–132.
[9] B. Syed, J. Geng, R.K. Mishra, K.S. Kumar, Scr. Mater. 67 (2012) 700–703.
[10] E. Lilleodden, Scr. Mater. 62 (2010) 532–535.
[11] C.M. Byer, B. Li, B. Cao, K.T. Ramesh, Scr. Mater. 62 (2010) 536–539.
[12] H. Yoshinaga, R. Horiuchi, Trans JIM 4 (1963) 1–8.
[13] Y. Tang, J.A. El-Awady, Acta Mater. 71 (2014) 319–332.
[14] B. Li, E. Ma, Philos. Mag. 89 (2009) 1223–1235.
[15] H. Fan, J.A. El-Awady, J. Appl. Mech. 82 (2015) 101006–101006.
[16] Z.H. Aitken, H. Fan, J.A. El-Awady, J.R. Greer, J. Mech. Phys. Solids 76 (2015) 208–223.
[17] H. Fan, S. Aubry, A. Arsenlis, J.A. El-Awady, Acta Mater. 92 (2015) 126–139.
[18] H. Fan, S. Aubry, A. Arsenlis, J.A. El-Awady, Scr. Mater. 97 (2015) 25–28.
[19] J. Zhang, K.T. Ramesh, S.P. Joshi, Model. Simul. Mater. Sci. Eng. 22 (2014) 075003.

[20] S. Plimpton, J. Comput. Phys. 117 (1995) 1–19.
[21] K.-H. Kim, J.B. Jeon, B.-J. Lee, Calphad 48 (2015) 27–34.
[22] B. Jelinek, S. Groh, M.F. Horstemeyer, J. Houze, S.G. Kim, G.J. Wagner, A. Moitra, M.I. Baskes, Phys. Rev. B 85 (2012) 245102.
[23] M. Ghazisaeidi, L.G. Hector Jr., W.A. Curtin, Scr. Mater. 75 (2014) 42–45.
[24] A. Stukowski, Model. Simul. Mater. Sci. Eng. 18 (2010) 015012.
[25] Y. Tang, J.A. El-Awady, Mater. Sci. Eng. A 618 (2014) 424–432.
[26] H. Fan, J.A. El-Awady, Q. Wang, J. Nucl. Mater. 458 (2015) 176–186.
[27] J. Chaussidon, M. Fivel, D. Rodney, Acta Mater. 54 (2006) 3407–3416.
[28] D.Y. Sun, M.I. Mendelev, C.A. Becker, K. Kudin, T. Haxhimali, M. Asta, J.J. Hoyt, A. Karma, D.J. Srolovitz, Phys. Rev. B 73 (2006) 024116.
[29] X.-Y. Liu, J.B. Adams, F. Ercolessi, J.A. Moriarty, Model. Simul. Mater. Sci. Eng. 4 (1996) 293.
[30] F.R.N. Nabarro, Mater. Sci. Eng. A 234–236 (1997) 67–76.
[31] Q. Yu, L. Qi, K. Chen, R.K. Mishra, J. Li, A.M. Minor, Nano Lett. 12 (2012) 887–892.
[32] H. Fan, S. Aubry, A. Arsenlis, J.A. El-Awady, Grain size effects on dislocation and twinning mediated plasticity in magnesium. Scr. Mater. Submitted (2015).
[33] J. Zhang, S.P. Joshi, J. Mech. Phys. Solids 60 (2012) 945–972.